Transport properties of polycrystalline $Mg_2Si_{1-y}Sb_y$ $(0 \leq y < 0.4)$

G. S. Nolas,* D. Wang, and M. Beekman
Department of Physics, University of South Florida, Tampa, Florida 33620, USA
(Received 27 July 2007; published 11 December 2007)

Thermal conductivity, Seebeck coefficient, resistivity, and Hall measurements on polycrystalline $Mg_2Si_{1-y}Sb_y$ with $0 \leq y \leq 0.37$ are reported. In these materials, Sb substitutes for Si in the antifluorite structure. As the Sb content increases, vacancies are formed in the lattice on Mg sites, which also contribute to variations in the transport properties. With increasing Sb content, both the absolute Seebeck coefficient and electrical resistivity first decrease, but then increase due to vacancy formation, while the thermal conductivity decreases monotonically with increasing Sb content. We investigate the lattice thermal conductivity by modeling the data using the Debye approximation in order to discern the contributions from different phonon-scattering mechanisms. We discuss the results in the context of potential thermoelectric applications.

DOI: 10.1103/PhysRevB.76.235204 PACS number(s): 72.20.Pa, 66.70.+f, 63.20.Mt

INTRODUCTION

Compounds with the antifluorite crystal structure (Mg_2E, where E=Si, Ge, or Sn) are covalently bonded semiconductors with relatively high mobilities and thermal conductivities.[1–5] They can readily be doped, Ag and Cu as electron acceptors, and Sb and Bi as donors,[6,7] and their intrinsic band gaps range from 0.77 eV for Mg_2Si to 0.36 eV for Mg_2Sn.[8] They possess properties that are similar to that of the group IV elemental semiconductors,[9] thus they have long been recognized as good candidates for thermoelectric applications.[8]

Recent reports of good thermoelectric properties[10] with high thermoelectric figures of merit, in addition to similar previous claims,[11,12] have added to the interest in this material system. The effectiveness of a material for thermoelectric applications is determined by the material's figure of merit, $ZT = S^2T/\kappa\rho$, where S is the Seebeck coefficient; κ is the thermal conductivity, which is composed of both lattice κ_L and electrical κ_e components; ρ is the electrical resistivity; and T is the absolute temperature. Typically, the power factor, S^2/ρ, is optimized as a function of carrier concentration through doping, and κ_L is reduced via alloying in order to give the largest ZT. A good thermoelectric material possesses a large S along with low ρ and κ. However, for a given material, these parameters are not independent.[13] Nevertheless, in certain bulk semiconducting and intermetallic compounds, a very low κ_L with relatively good electronic properties can provide high ZT values.[14] The antifluorite material system can be included in this category if κ_L can be substantially reduced without degrading the electrical properties. It has been demonstrated that Mg_3Sb_2 is soluble in Mg_2E, for E=Si, Ge, and Sn, up to 30%,[15–18] thus $(Mg_2E)_{1-x}(Mg_3Sb_2)_x$ mixed crystals with the antifluorite crystal structure are possible. These results indicate that a relatively high concentration of Sb can be substituted for Si in the antifluorite crystal structure. In previous studies, Sb or Bi was used as electrical dopant in small concentrations.[6,7] We examine the effect of incorporating high concentrations of Sb in Mg_2Si by evaluating the low temperature transport properties of polycrystalline $Mg_2Si_{1-y}Sb_y$. The influence of high concentrations of Sb within the antifluorite crystal structure is required in order to elucidate the structure-property relationships within this material system.

EXPERIMENTAL PROCEDURE

A series of seven $Mg_2Si_{1-y}Sb_y$ polycrystalline specimens was prepared for this investigation. Polycrystalline specimens were synthesized from high purity elements, in powder form, in stoichiometric amounts for the case of Si and Sb, and with an excess of 2 mol % from stoichiometry for Mg in order to compensate for the relatively high Mg vapor pressure. The powders were first mixed by grinding in a mortar and pestle, then cold pressed into solid pellets. The subsequent pellets were placed in tungsten crucibles that were sealed in quartz tubes in an Ar atmosphere and reacted at 570 °C for 24 h. After this initial solid-state reaction, the resulting pellets were ground to fine powders (utilizing a 325 mesh sieve) in a glovebox, cold pressed into pellets, and re-reacted under Ar at 850 °C (900 °C for the two specimens with the highest Sb content) for an additional 24 h. This latter step was repeated once more in order to ensure homogeneity. After this process, the resulting pellets were ground to fine powders and hot pressed at 20 000 lbs/in.^{2} and 800 °C for 2 h. Pieces of the hot pressed specimens were ground for x-ray powder diffraction (XRD) analysis. XRD was performed on a Bruker D8 Focus diffractometer using Cu $K\alpha$ radiation. Chemical compositions were determined by electron probe microanalysis (EPMA), averaged over several randomly selected locations within a section of each hot pressed polycrystalline pellet. For transport property measurements, the polycrystalline pellets were cut into parallelepipeds of size $2 \times 2 \times 5$ mm^3 using a wire saw to minimize surface damage. Steady state S and κ as well as four-probe ρ measurements were performed using a radiation-shielded vacuum probe in a custom-designed closed-cycle refrigerator. We employed a differential thermocouple to measure the temperature gradient, and 0.001 in. copper wires as voltage probes. Four-probe Hall measurements were carried out at room temperature employing a 2 T electromagnet. For Hall measurements, data were collected on $2 \times 0.5 \times 8$ mm^3 specimens at successive positive and negative magnetic fields to eliminate voltage probe misalign-

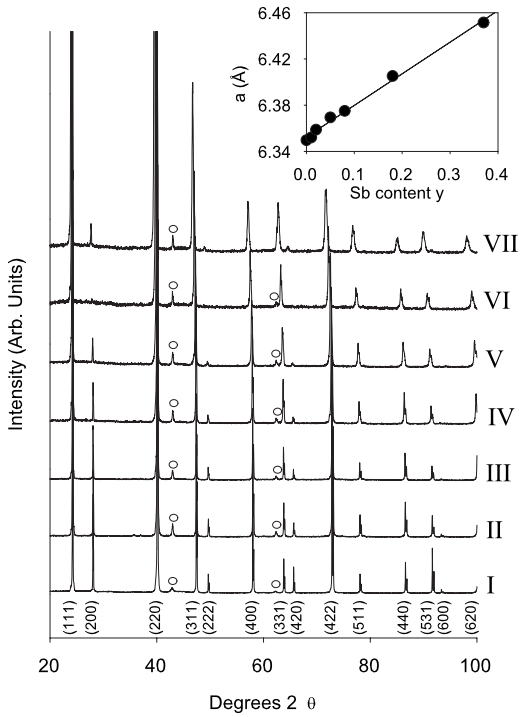

FIG. 1. XRD patterns for the seven polycrystalline antifluorite specimens synthesized. Miller indices (*hkl*) for reflections due to the antifluorite structure are indicated below the bottom pattern. Weak reflections due a trace amount (less than 1 wt %) of MgO present in the specimens are indicated by the symbol (○). Inset: Lattice parameter *a* estimated from powder XRD indicating a linear increase with Sb content.

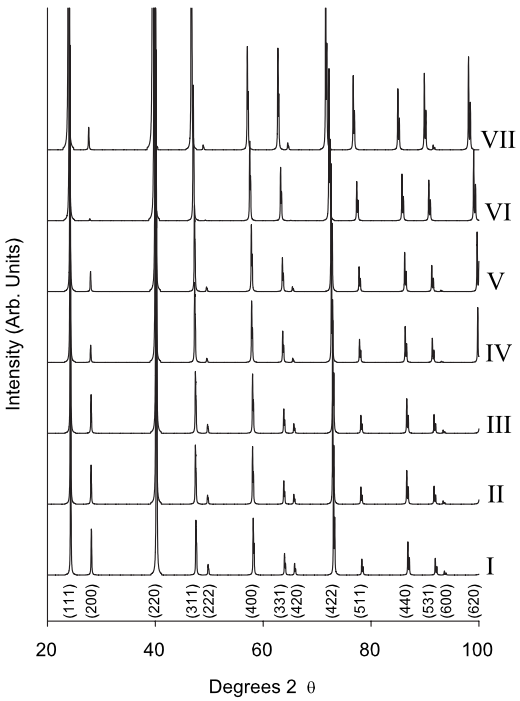

FIG. 2. Calculated XRD patterns for the seven antifluorite specimens, using site occupancies inferred by the stoichiometries listed in Table I. Miller indices (*hkl*) for reflections due to the antifluorite structure are indicated below the bottom pattern.

ment effects. Room temperature relative uncertainties for S, ρ, κ, and Hall are approximately 5%, 4%, 8%, and 10%, respectively.

RESULTS AND DISCUSSION

Figure 1 shows the XRD spectra, where the successive spectra are shifted in intensity for clarity and amplified to identify low intensity diffraction peaks corresponding to the trace amount of MgO impurity (estimated to be less than 1%) in the specimens. All other XRD peaks were indexed to the antifluorite (space group $Fm3m$) crystal structure. As shown in the inset of Fig. 1, the room temperature lattice parameters a increase linearly with Sb content. For the seven specimens prepared for this report, Table I lists the compositions determined from EPMA along with measured room temperature physical parameters. Elemental x-ray maps obtained from EPMA indicated the MgO phase to be located in isolated inclusions, and confirmed their fraction to be less than 1%, corroborating the results from powder x-ray diffraction shown in Fig. 1. We note that although Mg was prepared in excess of stoichiometric amounts, EPMA results indicate an increasing deficit of Mg as the Sb content increases above $y=0.05$, implying that Mg vacancies are present. Figure 2 displays calculated XRD powder patterns[19] obtained for the seven specimens. The patterns were calcu-

TABLE I. Compositions based on EMPA results, measured room temperature values for ρ, S, electron concentration n, and mobility μ, and estimated effective mass m_n^* (free electron effective mass=m_0).

Specimen No.	EMPA composition	ρ (mΩ cm)	S (μV/K)	n (cm^{-3})	μ (cm^2/V s)	m_n^*/m_0
I	$Mg_{2.05}Si$	71.6	−406	1.6×10^{18}	53	0.51
II	$Mg_{2.06}Si_{0.99}Sb_{0.01}$	1.7	−103	7.7×10^{19}	47	0.50
III	$Mg_{2.03}Si_{0.98}Sb_{0.02}$	1.0	−75	1.2×10^{20}	50	0.47
IV	$Mg_{2.03}Si_{0.95}Sb_{0.05}$	1.1	−71	1.6×10^{20}	36	0.52
V	$Mg_{1.99}Si_{0.92}Sb_{0.08}$	1.8	−68	1.8×10^{20}	20	0.50
VI	$Mg_{1.95}Si_{0.82}Sb_{0.18}$	2.1	−75	1.6×10^{20}	18	0.55
VII	$Mg_{1.81}Si_{0.63}Sb_{0.37}$	7.6	−102	5.9×10^{19}	14	0.41

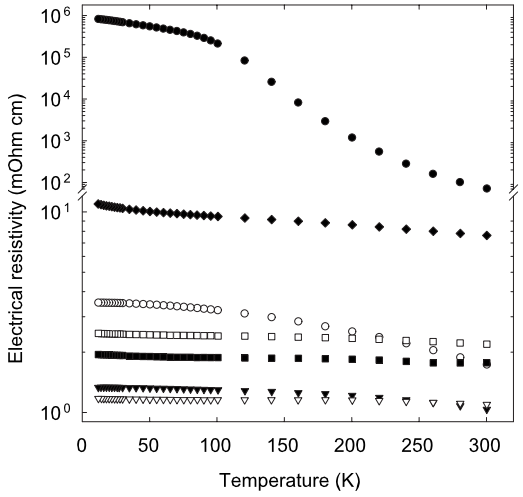

FIG. 3. Temperature dependence of resistivity for the seven specimens listed in Table I. The symbols correspond to the specimens as follows: I (●), II (○), III (▼), IV (▽), V (■), VI (□), and VII (◆).

lated using the experimentally determined lattice parameters, with site occupancies inputted taking into consideration the compositions shown in Table I. The agreement between the experimental and calculated power XRD patterns indicates that Mg vacancies as well as Sb substitution for Si are present in our specimens. Specifically, the relative increase or decrease in the intensities of several reflections [for example, the (200), (311), (222), and (420) reflections] in the range 20°–70° 2θ corroborates well with the experimental patterns (Fig. 1). This compositional variation indicated from both EPMA and powder XRD also has a direct effect on the transport, as we will discuss in detail below.

Temperature dependent ρ and S data for all seven specimens are plotted in Figs. 3 and 4, respectively. Room temperature ρ values (Table I) range from 1.0 to 7.6 mΩ cm for the Sb doped compositions and an order of magnitude higher

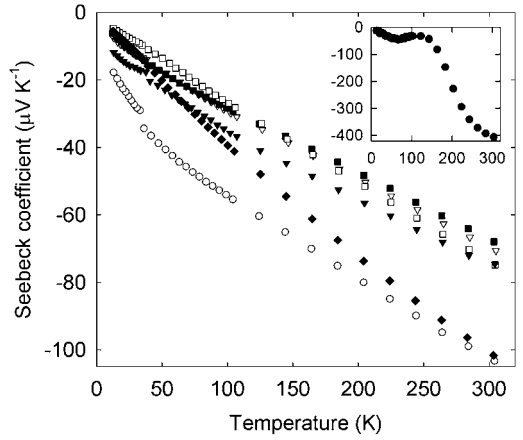

FIG. 4. Temperature dependence of the Seebeck coefficient for the seven specimens listed in Table I. The symbols correspond to the same specimens as in Fig. 3. Inset: Temperature dependence of S for undoped Mg_2Si (specimen I; same units as the main figure).

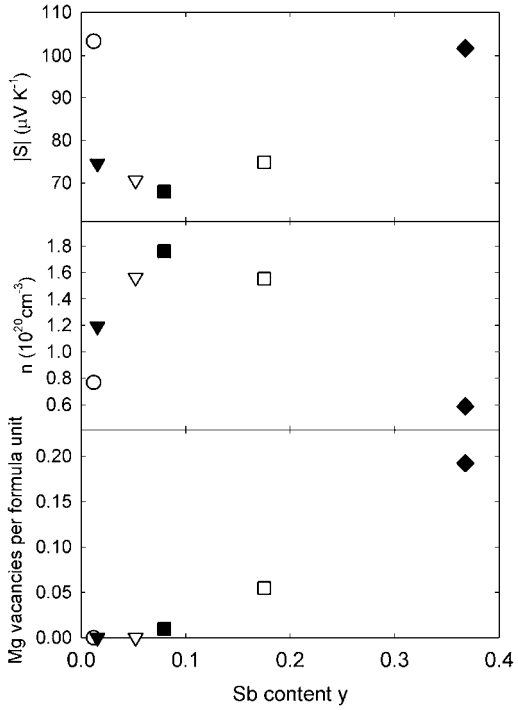

FIG. 5. Number of vacancies per formula unit on the Mg site, along with room temperature carrier concentration and absolute Seebeck coefficient, as a function of Sb content y for $Mg_2Si_{1-y}Sb_y$.

for Mg_2Si. The materials with $y>0$ display a relatively flat temperature dependence; however, the room temperature values show an initial decrease in resistivity with Sb content, reaching a minimum for $y=0.02$ before increasing as y further increases. This trend is similar to that shown in Fig. 4, where at room temperature $|S|$ (the absolute value of S) first decreases with y, reaches a minimum at $y=0.08$, and then increases. Room temperature S values range between −68 and −103 μV/K for the Sb doped specimens.

Hall and S measurements combined with EPMA analyses help elucidate the nature of these trends. Figure 5 shows room temperature carrier concentration and $|S|$ as a function of Sb content. An increasing (decreasing) carrier concentration results in a decreasing (increasing) $|S|$, as expected for typical extrinsic semiconductor behavior. The maximum carrier concentration, as well as minimum $|S|$, is obtained for $y\sim0.08$. Applying a simple crystal chemistry approach, one would expect a monotonic increase in carrier concentration upon Sb substitution for Si. However, Fig. 5 clearly indicates that this is not the case above $y=0.08$. We eliminate the possibility of band curvature modification with increasing Sb in these materials (*vide infra*) as the reason for this effect, but note the Mg-site vacancies determined by the EPMA data as the origin. This is also illustrated in Fig. 5, where Mg vacancies from EPMA results (Table I) as a function of Sb content are shown. At low Sb concentrations, there is no direct vacancy formation and Sb acts as an electron donor; however, at higher Sb concentrations, vacancies are increasingly created on the Mg sites. These vacancies can create electron acceptor states, and thus, begin to compete with the contribution from Sb donors. The higher the Sb content, therefore,

the larger the vacancy concentration. The overall effect results in a decrease in electron concentration above $y=0.08$, although S and Hall measurements indicate electrons as majority carriers for all compositions. In previous work on Sb and Bi doping of Mg_2E,[6,7] only low concentrations of these elements were doped in Mg_2E; thus, this effect was not observed. This vacancy formation also results in lower mobilities, as shown in Table I, which contributes to increasing ρ as the concentration of vacancies increases.

From room temperature S, ρ, and Hall carrier concentration, we can also estimate the electron effective mass in these materials. As indicated in Table I, the six compositions are heavily doped semiconductors. Extrinsic alloys and doped antifluorite compounds have shown strong electron-acoustic phonon scattering behavior,[5] as has been observed in other material systems.[20,21] We, therefore, expect a mixed ionized impurity and acoustic phonon scattering for electrons near room temperature. Assuming a single parabolic band, S and n are given by[21]

$$S = \pm \frac{k_B}{e}\left[\frac{(2+r)F_{1+r}(\eta)}{(1+r)F_r(\eta)} - \eta\right] \tag{1}$$

$$n = \frac{\sqrt{2}}{\pi^2}\left[\frac{m_n^* k_B T}{\hbar^2}\right]^{3/2} F_{1/2}(\eta), \tag{2}$$

where r is the exponent of the energy dependence of the electron mean free path, m_n^* is the electron effective mass, e is the electron charge, $\eta=E_F/k_BT$ is the reduced Fermi energy, E_F is the Fermi energy, and $F_i(\eta)$ is the Fermi integral of order i. The + and − signs in Eq. (1) are appropriate for holes and electrons, respectively. Table I lists the estimated m_n^* values using $r=1$ for mixed scattering from ionized impurities and acoustic phonons. These values are in good agreement with those reported previously for Mg_2Si,[22] and indicate negligible modification of the band curvature and that the vacancies on the Mg site lead to the variations in electrical transport.

Figure 6 shows temperature dependent κ_L data. We estimate κ_L using the Wiedemann-Franz relation ($\kappa_L=\kappa-\kappa_e$, where $\kappa_e=L_0T/\rho$ with $L_0=2.45\times10^{-8}$ V^2 K^{-2}) using our measured values for ρ. As shown in Fig. 6, κ_L decreases, and the peak in κ_L also decreases, with increasing Sb content. The composition with the highest Sb content results in a reduction in room temperature κ_L of over a factor of 6 as compared to that of Mg_2Si, while the peak κ_L value is reduced by over a factor of 30. The solid lines in Fig. 6 are theoretical fits to the data using the Debye approximation[23]

$$\kappa_L = \frac{k_B}{2\pi^2 v}\left(\frac{k_B T}{\hbar}\right)^3 \int_0^{\theta_D/T} \frac{x^4 e^x}{\tau_C^{-1}(e^x-1)^2} dx, \tag{3}$$

where $x=\hbar\omega/k_BT$ is dimensionless, ω is the phonon frequency, k_B is the Boltzmann constant, $\hbar$ is the reduced Planck constant, θ_D is the Debye temperature, v is the speed of sound, and τ_C is the phonon-scattering relaxation time. The phonon-scattering relaxation rate τ_C^{-1} can be written as $\tau_C^{-1}=v/L+A\omega^4+B\omega^2T\exp(-\theta_D/3T)$, where L is the grain size and the coefficients A and B are the fitting parameters.

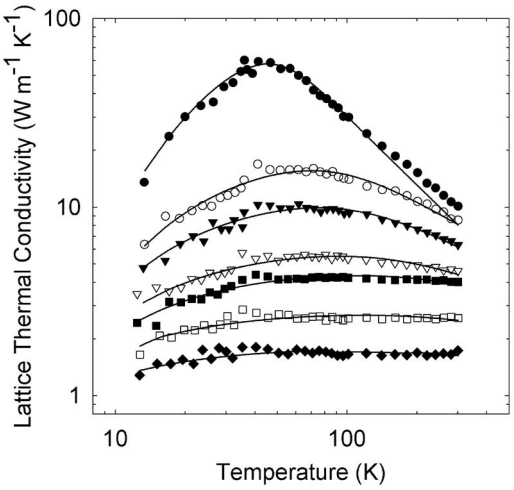

FIG. 6. Temperature dependent lattice thermal conductivity for the seven specimens listed in Table I. The symbols correspond to the same specimens as in the previous figures. The solid lines are calculated fits based on Eq. (3).

The three terms for τ_C^{-1} represent grain boundary scattering, point defect scattering, and phonon-phonon umklapp scattering, respectively. The expression for umklapp scattering is essentially empirical. θ_D and v $[=(1/3v_L^3+2/3v_T^3)^{1/3}]$ values for Mg_2Si were used in our fitting, and are 542 K and 5063 m/s,[22] respectively. The solid lines fit the data well for all specimens over the entire temperature range. From our theoretical fits, we obtain the fitting parameters shown in Table II.

The grain size L is in relatively good agreement with the experimentally determined grain sizes estimated for these specimens, ranging from 10 to 20 μm from scanning electron microscope images of polished surfaces. The B prefactors are somewhat similar within the specimens, while differing from that for Mg_2Si. As we do not know the Debye temperature and Grüneisen constant for these compositions, parameters that influence B,[24] we cannot quantitatively compare a dependence on B between Mg_2Si and the Sb containing compositions.

From Table II and Fig. 6, it is reasonable to presume that alloy scattering, indicated by prefactor A, is an important phonon-scattering mechanism in these materials. The magnitude of prefactor A increases as the Sb concentration increases, with an almost 3 orders of magnitude increase from specimen I to specimen VII. This is an indication that alloy scattering increases dramatically with Sb content. The prefactor A is defined as[23]

$$A = \frac{V\Gamma}{4\pi v^3}, \tag{4}$$

where V is the volume of the primitive cell ($a^3/4$ for the face-centered antifluorite structure) and Γ is the scattering parameter. Γ can then be experimentally obtained ($\Gamma=\Gamma_{exp}$) from Eq. (4). We can also calculate Γ for mass-fluctuation scattering alone (Γ_{mass}) for the seven compositions using[23,25]

TABLE II. Values of lattice thermal conductivity fit parameters as defined by Eqs. (3)–(5) and in the text, for the seven specimens listed in Table I.

Specimen	Sb content y	L (10^{-6} m)	A (10^{43} s^3)	B (10^{-18} s K^{-1})	Γ_{exp}	Γ_{mass}	$\Gamma_{exp}-\Gamma_{mass}$
I	0	7.5	1.4	5.44	0.004	0	0.004
II	0.01	7.1	15.9	1.58	0.040	0.043	−0.003
III	0.02	9.4	35.7	1.20	0.091	0.084	0.007
IV	0.05	11.7	94.0	0.64	0.237	0.189	0.048
V	0.08	12.8	138.5	0.35	0.349	0.281	0.067
VI	0.18	29.1	367.2	0.21	0.911	0.488	0.423
VII	0.37	45.9	766.0	0.20	1.861	0.641	1.220

$$\Gamma_{mass} = \frac{1}{3}\left[2f_{\mathrm{Mg}} f_{vacancy} \left(\frac{M_{\mathrm{Mg}} - M_{vacancy}}{\bar{M}} \right)^2 + f_{\mathrm{Si}} f_{\mathrm{Sb}} \left(\frac{M_{\mathrm{Si}} - M_{\mathrm{Sb}}}{\bar{M}} \right)^2 \right], \quad (5)$$

where f_{Mg}, $f_{vacancy}$, f_{Si}, and f_{Sb} are the fractional occupancies (as determined from EPMA; see Table II); M_{Mg}, $M_{vacancy}$, M_{Si}, and M_{Sb} are the respective constituent masses ($M_{vacancy}=0$); and $\bar{M}$ is the average mass of the compound. The results are given in Table II, and indicate that for small Sb concentrations ($y<0.08$), $\Gamma_{exp}\sim\Gamma_{mass}$, indicating the majority of alloy phonon scattering is due to the difference in mass between Sb and Si. As the Sb concentration increases, Γ_{exp} becomes significantly larger than Γ_{mass}, implying that there is a scattering mechanism other than mass-fluctuation scattering that not only contributes to the reduction in κ_L, but is dominant in the compositions with higher Sb concentrations. Figure 5 revealed that the number of vacancies increases rapidly at higher Sb concentrations. It is reasonable to assume a substantial strain-field scattering due to these vacancies ($\Gamma_{strain}=\Gamma_{exp}-\Gamma_{mass}$, shown in Table II). We note that the strain-field contribution from Sb substitution for Si will also contribute to the κ_L reduction; however, vacancies result in a large localized lattice strain and have a larger effect on κ_L. A similar phenomenon has also been observed in some oxides. In $Zr_{0.8}Y_{0.2}O_{0.9}$, for example, vacancies are generated on the O sites by substituting Y^{3+} for Zr^{4+}, resulting in the suppression of κ_L (Refs. 26–28) that was attributed to vacancy formation.[29]

CONCLUSIONS

We have investigated the role of Sb doping, from low to relatively high concentrations, in Mg_2Si. Antimony acts as an electron donor in this material system at low concentration, but creates vacancies at higher concentration. These vacancies act as electron acceptors, thus modifying the electronic transport properties. The vacancies also act as strong phonon-scattering centers; the composition with the highest Sb content resulted in a reduction in room temperature κ_L of over a factor of 6 as compared to that of Mg_2Si, while the peak κ_L value was reduced by over a factor of 30. These results confirm that Sb can be a useful dopant for n-type antifluorite materials; however, for higher concentrations of Sb, the resulting Mg vacancies contribute negatively to optimizing the transport properties for thermoelectric applications.

ACKNOWLEDGMENTS

The authors acknowledge support by GM and DOE under corporate agreement DE-FC26-04NT42278. M.B. acknowledges support from the University of South Florida.

*gnolas@cas.usf.edu

[1] U. Winkler, Helv. Phys. Acta **28**, 633 (1955).
[2] R. G. Morris, R. D. Redin, and G. C. Danielson, Phys. Rev. **109**, 1909 (1958).
[3] R. D. Redin, R. G. Morris, and G. C. Danielson, Phys. Rev. **109**, 1916 (1958).
[4] B. Lichter, J. Electrochem. Soc. **109**, 819 (1962).
[5] J. J. Martin, J. Phys. Chem. Solids **33**, 1139 (1972).
[6] J. Tani and H. Kido, Physica B **364**, 218 (2005).
[7] J. Tani and H. Kido, Intermetallics **15**, 1202 (2007).
[8] V. K. Zaitsev, M. I. Fedorov, I. S. Eremin, and E. A. Gurieva, *Thermoelectrics Handbook* (CRC, Boca Raton, FL, 2006), Chap. 29.
[9] J. L. Corkill and M. L. Cohen, Phys. Rev. B **48**, 17138 (1993).
[10] V. K. Zaitsev, M. I. Fedorov, E. A. Gurieva, I. S. Eremin, P. P. Konstantinov, A. Y. Samunin, and M. V. Vedernikov, Phys. Rev. B **74**, 045207 (2006).
[11] R. J. LaBotz, D. R. Mason, and D. F. O'Kane, J. Electrochem. Soc. **110**, 127 (1963).
[12] Y. Noda, H. Kon, Y. Furukawa, N. Otsuka, I. A. Nishida, and K. Masumoto, Mater. Trans., JIM **33**, 851 (1992).
[13] G. S. Nolas, J. Sharp, and A. H. J. Goldsmid, *Thermoelectrics: Basic Principles and New Materials Developments* (Springer,

New York, 2001).
[14] G. S. Nolas, J. Poon, and M. Kanatzidis, MRS Bull. **31**, 199 (2006).
[15] K. A. Bol'shakov, N. A. Bul'onkov, L. N. Rastorguev, and M. S. Tsirlin, Russ. J. Inorg. Chem. **8**, 1418 (1963).
[16] K. A. Bolshakov, N. A. Bulonkov, L. N. Rastorguev, Y. S. Umanskii, and M. S. Tsirlin, Russ. J. Inorg. Chem. **8**, 2710 (1963).
[17] N. A. Bulyaev, V. V. Saharov, and O. Sh. Goggishuili, Inorg. Mater. **6**, 1744 (1970).
[18] G. S. Nolas, D. Wang, and X. N. Lin, Phys. Status Solidi (RRL) **1**, 223 (2007).
[19] W. Kraus and G. Nolze, POWDERCELL 2.4 for Windows, 2000.
[20] For example, in skutterudites [G. S. Nolas, D. T. Morelli, and T. M. Tritt, Annu. Rev. Mater. Sci. **29**, 89 (1999)].
[21] G. A. Slack and M. A. Hussain, J. Appl. Phys. **70**, 2694 (1991).
[22] *Semiconductors: Physics of Non-Tetrahedrally Bonded Elements and Binary Compounds I*, edited by K.-H. Hellwege and O. Madelung, Landolt-Börnstein, New Series, Group III, Vol. 17, Pt. E (Springer-Verlag, Berlin, 1983), p.164.
[23] See, for example, *Thermal Conductivity: Theory, Properties, and Applications*, edited by T. M. Tritt (Kluwer Academic, New York, 2004).
[24] G. A. Slack, in *Solid State Physics*, edited by F. Seitz and D. Turnbull (Academic, New York, 1979), Vol. 34, p. 1.
[25] J. Yang, G. P. Meisner, and L. Chen, Appl. Phys. Lett. **85**, 1140 (2004).
[26] D. G. Cahill, S. K. Watson, and R. O. Pohl, Phys. Rev. B **46**, 6131 (1992).
[27] J. Bisson, D. Fournier, M. Poulain, O. Lavigne, and R. Mévrel, J. Am. Ceram. Soc. **83**, 1993 (2000).
[28] M. R. Winter and D. R. Clarke, Acta Mater. **54**, 5051 (2006).
[29] P. G. Klemens, in *Thermal Conductivity* (Technomic, Lancaster, PA 1996), Vol. 23, p. 209.